Cell Reports

Heterogeneous Habenular Neuronal Ensembles during Selection of Defensive Behaviors

Graphical Abstract

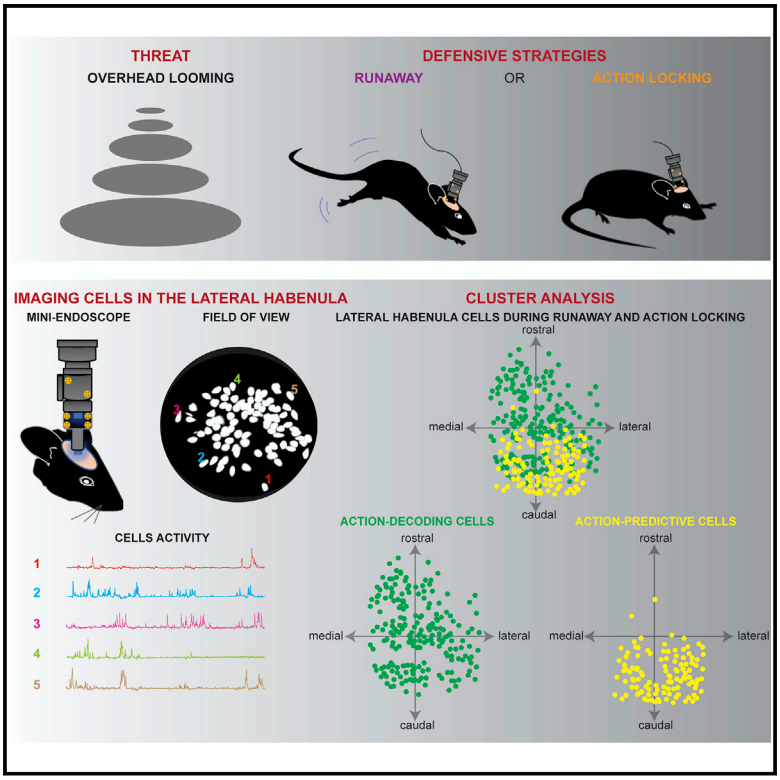

Highlights

- A threat promotes opposing and context-dependent behavioral responses
- Habenular neurons encode looming-driven runaway and action-locking
- Habenular clusters define different time epochs of defensive behaviors

Authors

Salvatore Lecca, Vijay M.K. Namboodiri, Leonardo Restivo, Nicolas Gervasi, Giuliano Pillolla, Garret D. Stuber, Manuel Mameli

Correspondence

salvatore.lecca@unil.ch (S.L.), manuel.mameli@unil.ch (M.M.)

In Brief

Lecca et al. show that the lateral habenula (LHb) underlies threat-driven defensive behaviors in mice. LHb calcium dynamics increase when mice run away and decrease when mice remain immobile upon a threat presentation. Distinct cell clusters emerge in LHb during defensive strategies: some representing the action and others holding predictive power.

Lecca et al., 2020, Cell Reports *31*, 107752
June 9, 2020
https://doi.org/10.1016/j.celrep.2020.107752

Cell Reports

CellPress
OPEN ACCESS

Report

Heterogeneous Habenular Neuronal Ensembles during Selection of Defensive Behaviors

Salvatore Lecca,[1,*] Vijay M.K. Namboodiri,[2] Leonardo Restivo,[1] Nicolas Gervasi,[3] Giuliano Pillolla,[4] Garret D. Stuber,[2] and Manuel Mameli[1,5,6,*]

[1]The Department of Fundamental Neuroscience, The University of Lausanne, 1005 Lausanne, Switzerland
[2]Center for the Neurobiology of Addiction, Pain, and Emotion, Department of Anesthesiology and Pain Medicine, Department of Pharmacology, University of Washington, Seattle, WA 98195, USA
[3]College de France, INSERM, 75005 Paris, France
[4]The University of Cagliari, 09042 Cagliari, Italy
[5]INSERM, UMR-S 839, 75005 Paris, France
[6]Lead Contact
*Correspondence: salvatore.lecca@unil.ch (S.L.), manuel.mameli@unil.ch (M.M.)
https://doi.org/10.1016/j.celrep.2020.107752

SUMMARY

Optimal selection of threat-driven defensive behaviors is paramount to an animal's survival. The lateral habenula (LHb) is a key neuronal hub coordinating behavioral responses to aversive stimuli. Yet, how individual LHb neurons represent defensive behaviors in response to threats remains unknown. Here, we show that in mice, a visual threat promotes distinct defensive behaviors, namely runaway (escape) and action-locking (immobile-like). Fiber photometry of bulk LHb neuronal activity in behaving animals reveals an increase and a decrease in calcium signal time-locked with runaway and action-locking, respectively. Imaging single-cell calcium dynamics across distinct threat-driven behaviors identify independently active LHb neuronal clusters. These clusters participate during specific time epochs of defensive behaviors. Decoding analysis of this neuronal activity reveals that some LHb clusters either predict the upcoming selection of the defensive action or represent the selected action. Thus, heterogeneous neuronal clusters in LHb predict or reflect the selection of distinct threat-driven defensive behaviors.

INTRODUCTION

When facing an external threat, animals select from a repertoire of innate behavioral responses, ranging from escape (runaway) to immobile-like (action-locking) strategies (Evans et al., 2019). These behaviors ultimately increase individual survival, rely on the external environment, and can be adopted by the same animal (Blanchard et al., 2011; De Franceschi et al., 2016; Eilam, 2005). The detection of a threat and the optimal selection of such threat-driven actions (i.e., runaway or action-locking) require the coordination of complex brain networks. The recent analysis of threat-driven escape behaviors unraveled the essential contribution of neuronal circuits, including the amygdala, the superior colliculus, the periaqueductal gray, the hypothalamus, or the midbrain. All of these are pivotal neuronal nodes for aversive processing (Evans et al., 2018; Headley et al., 2019; Silva et al., 2016; Tovote et al., 2016; Zhou et al., 2019). Neurons located in the epithalamic lateral habenula (LHb) signal the negative valence of a stimulus contributing to aversive behaviors (Matsumoto and Hikosaka, 2007). Accordingly, habenular neurons in fish, rodents, and non-human primates, as opposed to midbrain dopamine neurons, respond mainly with excitation to a variety of aversive stimuli and reduce their activity after reward presentation (Andalman et al., 2019; Lecca et al., 2017; Matsumoto and Hikosaka, 2007; Wang et al., 2017). Specifically, aversion-driven LHb neuronal excitation requires hypothalamic glutamate release to shape behavioral responses upon unexpected and predicted aversive events (Lazaridis et al., 2019; Lecca et al., 2017; Trusel et al., 2019). Reducing the efficacy of hypothalamus-to-LHb projections impairs behavioral escape driven by foot shocks, shock-predicting cues, and predator-like looming stimulus (Lecca et al., 2017; Trusel et al., 2019). The latter evidence indicates a relevant contribution of LHb in encoding environmental threats. However, whether specific neuronal representations in the LHb participate in the selection of threat-driven defensive behaviors (runaway or action-locking) remains unknown.

To examine this question, we performed deep-brain Ca^{2+} imaging of large LHb neuronal populations using a head-mounted miniaturized microscope in mice engaging visual threat-driven defensive responses (Resendez et al., 2016). We combined such large-scale recordings with unsupervised classification of response patterns. This led to the identification of functionally distinct LHb neuronal subpopulations during threat-driven runaway and action-locking. Analysis of responses indicates that multiple neuronal clusters emerge during

behavioral strategies holding independent information (i.e., prediction versus action) related to the temporal expression of the behaviors. These data support the participation of LHb neuronal populations in the selection of defensive behaviors when facing an external threat.

RESULTS

Opposing Behavioral Strategies in Response to a Visual Threat

Ethological studies posit a relationship between the animal-nest distance and the strategy adopted to react to a threat (Blanchard et al., 2005, 2011). The closer to a nest, the more likely it is for animals to rapidly run away to hide. Action-locking responses, instead, occur with higher frequency when the animal is located far from the shelter (Yilmaz and Meister, 2013).

Here, we investigated these independent threat-driven behavioral strategies in mice using an innately aversive overhead expanding spot (looming) (Yilmaz and Meister, 2013), while mice explore an experimental arena provided with a nest. We randomly triggered the looming stimulus when the mouse explored different zones of the arena with variable distance with respect to the nest (Figures 1A, 1B, and S1A). Mice predominantly adopted threat-driven high-speed runaway responses (Figures 1A–D and S1A). In a smaller fraction of trials, however, the same animals engaged in a looming-driven action-locking, a behavior outlined by significant speed reduction (Figures 1A–D). Such opposite looming-driven behavioral strategies related to the distance from the nest (Figure 1D) and the imminence of the threat as higher probability of action-locking occurred within the area outside the looming shadow (Figure S1A). Multiple looming presentations revealed stable and comparable average onset time between runaway and action-locking responses, yet different offset timing, with action-locking events lasting up to tens of seconds (Figures 1E and S1B). Mice can display divergent defensive behaviors to the same visual threat stimulus in a context-dependent fashion.

Threat Encoding in the LHb

Next, we used fiber photometry to measure fluorescent calcium transients (Ca^{2+}; Cui et al., 2014) and examined the population dynamics of LHb neurons in freely behaving mice (Figure 2A). We injected rAAV2.5-hSyn1-GCaMP6f into the LHb and implanted an optical fiber above the injection site (Figures 2A and S2A). The onset of threat-driven runaway occurred along with a robust increase in Ca^{2+} fluorescence from LHb neurons (Figures 2A and 2B; Video S1). In contrast, looming-driven action-locking developed together with a reduction in LHb fluorescence (Figures 2A and 2B; Video S2). Notably, a significant shift in fluorescence emerged time-locked with the visual looming stimulus and before the behavior (Figures S2B and S2C). The magnitude of this fluorescence increase was comparable between runaway and action-locking trials (Figures S2B and S2C). Signal magnitude was statistically larger only when the looming projection occurred above the animal (modeling a predator attack), but not from the frontal position (Figures S2D–S2F). This argues that the LHb signal encodes threats, not exclusively the visual stimulus. Both runaway and action-locking occurred along with an abrupt change in speed at the behavioral onset (Figure 1C). However, speed changes outside the looming presentation did not coincide with fluorescence transients, supporting the idea that spontaneous locomotion does not engage LHb activity (Figures S2G and S2H; Lecca et al., 2017). The observation that no fluorescence transients occurred in animals injected only with a rAAV2.5-hSyn1-GFP supports the specificity of signal detection (Figures S2I and S2L). Perturbing LHb activity (time-locked with looming) through the activation of the inhibitory opsin Jaws (rAAV2.8-hSyn-Jaws-GFP) impaired defensive strategies (Figures 2C, 2D, and S3A–S3G; Video S3). These data suggest that a threat recruits differential LHb neuronal responses throughout the expression of diverse behavioral strategies.

Heterogeneity of Habenular Neuronal Activity Emerges during Defensive Behaviors

Analysis of neuronal function with fiber photometry (Figures 2A and 2B) lacks cellular-level resolution and provides only aggregated activity from large neuronal populations (Resendez et al., 2016). Such limitation can be circumvented through the use of gradient-refractive-index (GRIN) lenses, which enable the visualization of deep-brain neuronal activity with single-cell resolution. We next examined how individual LHb neurons represent threats via their activity patterns. We used a miniature fluorescence microscope to track the relative changes in Ca^{2+} fluorescence in LHb neurons in freely moving mice during threat-driven behaviors (Figure 3A; 62 ± 14.6 neurons per animal; $n_{mice} = 4$). LHb neurons exhibited diverse activity patterns, with sharp elevations in Ca^{2+} fluorescence during runaway. The response was in the opposite direction during action-locking trials (Figures 3B, S4A, and S4B; Video S4). Thus, single-cell analysis of the Ca^{2+} signal indicates that opposite neuronal responses in the LHb reflect independent threat-driven behavioral strategies.

Individual LHb cells displayed variable profiles of runaway-excited/action-locking inhibited responses (Figures S4A and S4B). Furthermore, the activity of single neurons during a given defensive strategy across trials was also variable (Figure S4C). This argues in favor of functional heterogeneity across LHb neuronal responses after threat. We used an unsupervised clustering algorithm to group the trial-averaged time-locked response of each cell after runaway and action-locking onset ($n = 248$ from $n = 4$ mice; Figures 3C and S4D). This analysis revealed 8 clusters of neurons based on their responses surrounding the behavioral onset (Figures 3C, S4D, and S4E). Clusters were represented in each animal, supporting the strength of independent neuronal representations (Figure S4F). The responses of clusters 1–5 qualitatively recapitulated fiber photometry Ca^{2+} dynamics time-locked to runaway and action-locking onset (Figure 3C). Clusters 7 and 8 instead were weakly modulated during looming-triggered defensive responses. Clusters 3 and 6 stood out as their pre-action Ca^{2+} dynamics discriminated the upcoming behavior (Figure 3C). LHb clusters activity was not influenced by spontaneous locomotion (Figure S4H). This supports the existence of distinct clusters of individual neurons participating throughout threat-driven behavioral responses.

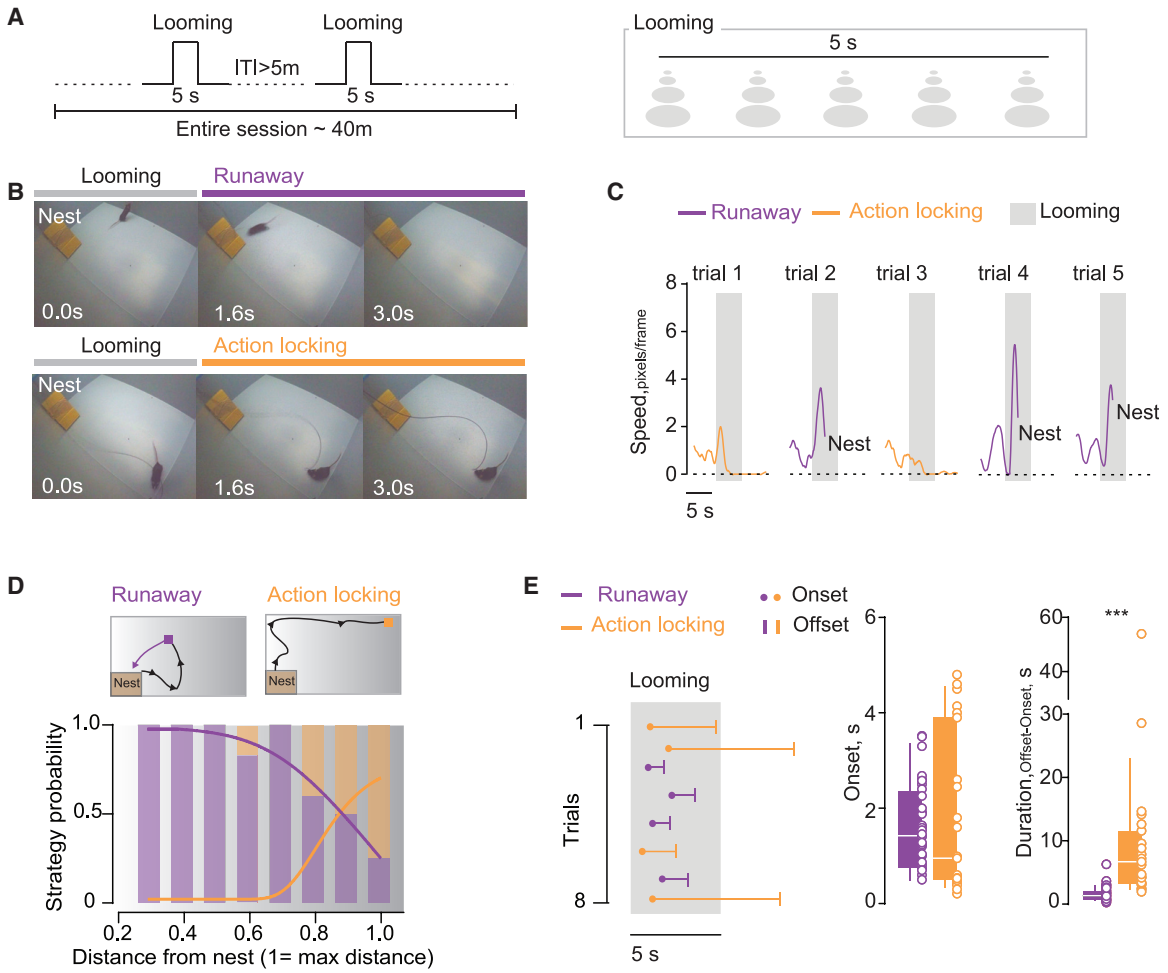

Figure 1. Threat Exposure Promotes Divergent Defensive Strategies

(A) Schematic of the looming protocol.

(B) Extracted video frames depicting a mouse during looming-driven runaway (top) and action-locking (bottom).

(C) Representative single mouse runaway and action-locking trials to multiple looming stimuli.

(D) Top: representative track of a single mouse during runaway and action-locking trials. Bottom: strategy probability in the function of the mouse-nest distance ($n_{runaway\ trials}$ = 56; $n_{action\text{-}locking\ trials}$ = 23; n_{mice} = 11; mouse-nest distance (maximum distance = 1): runaway trials versus action-locking trials; 0.3: 4 versus 0; 0.4: 7 versus 0; 0.5: 8 versus 0; 0.6: 10 versus 2; 0.7: 11 versus 0; 0.8: 9 versus 6; 0.9: 3 versus 3; 1.0: 4 versus 12; X^2_7 = 31.68; ***p < 0.0001, chi-square test). The lines fitting a sigmoidal distribution reports the correlation between the mouse-nest distance and the selected strategy (runaway: r = −0.883, R^2 = 0.78, **p = 0.003; action-locking: r = 0.884, R^2 = 0.78, **p = 0.003, Pearson correlation coefficient).

(E) Left: single mouse runaway (purple) and action-locking (orange) time frame reported for each trial (dot: onset response, line: offset response). Right: pooled data ($n_{runaway\ trials}$ = 56; $n_{action\text{-}locking\ trials}$ = 23) for onset (runaway versus action-locking; 1.631 ± 0.14 versus 1.797 ± 0.34 s; t_{77} = 0.53; p = 0.59, unpaired t test) and duration (runaway versus action-locking; 1.52 ± 0.14 versus 9.58 ± 2.37 s; t_{77} = 5.29; ***p < 0.0001, unpaired t test) of runaway and action-locking.

Data are presented with boxplots (median and 10th–90th quartile) or means ± SEMs.

See also Figure S1.

Decoding the Contribution of Habenular Clusters to Threat-Driven Behaviors

The existence of clusters with neuronal activity that distinguishes the defensive behaviors before the onset of the action (especially clusters 3 and 6) raised the intriguing possibility that LHb neurons may predict the upcoming selection of runaway or action-locking. To test this idea, we examined the neuronal coding of LHb ensembles by testing whether the defensive strategy on a given trial was identifiable from individual neuron activity patterns (Figure 4A). We defined 3 time epochs as "prediction of action" (−3 to 0 s from action), "immediate action" (0–3 s from action), and "delayed action" (3–6 s from action) (Figure 4B). Using leave-one-out cross-validation of a naive Bayes classifier (Namboodiri et al., 2019), we calculated the decoding accuracy per neuron above the chance decoding obtained when shuffling trial identity. We then averaged these accuracies across all recorded neurons (Figure 4C) or across all neurons within a cluster (Figure 4D). The null hypothesis was that the average decoding accuracy (above chance) per time frame and (sub)population is zero. We found that the average decoding accuracy across

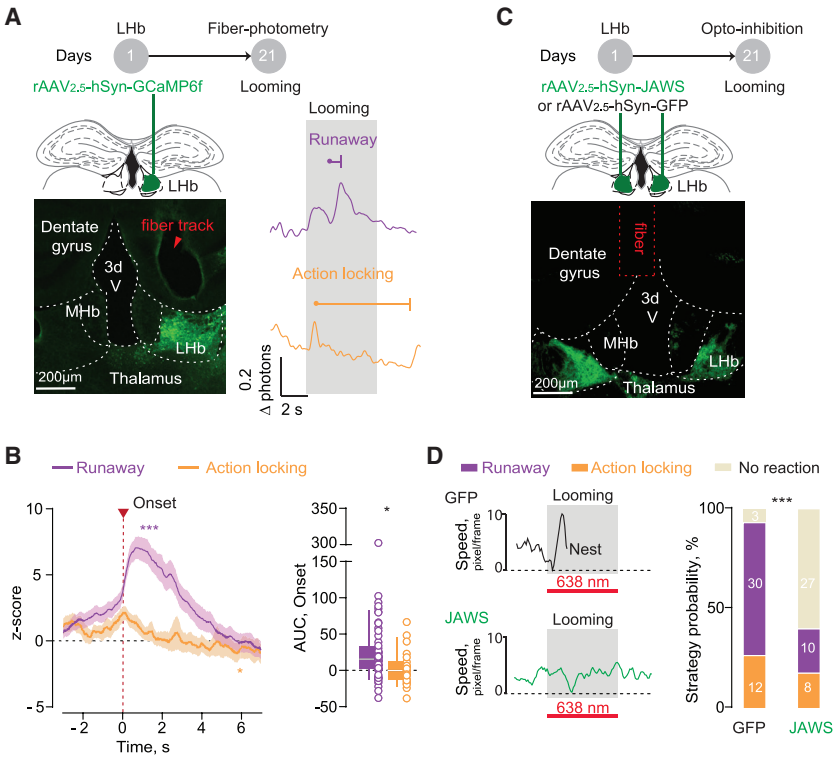

Figure 2. Divergent Habenular Neuronal Dynamics Underlying Threat-Driven Behaviors

(A) Top: schematic of the experiment. Bottom left: representative brain coronal section showing GCamp6f transduction and the fiber implantation track in the LHb. Bottom right: representative Ca^{2+} traces during runaway (red, top) and action-locking (blue, bottom) trials (looming, gray bar).

(B) Time course of averaged traces and boxplots reporting respectively *Z* score (runaway = 56 trials, $F_{3,850} = 40.5$, ***$p < 0.0001$; action-locking = 23 trials, $F_{1,540} = 3.122$, *$p = 0.033$; repeated measures (RM) 1-way ANOVA) and area under the curve (runaway versus action-locking, 26.14 ± 6.56 versus 3.05 ± 5.0; $t_{77} = 2.10$, *$p = 0.039$, unpaired t test) for single trials aligned to the behavioral onset.

(C) Top: schematic of the experiment. Bottom: representative brain coronal section showing Jaws transduction in LHb and fiber placement above it.

(D) Representative speed traces in a GFP-injected (top) and a Jaws-injected mouse (bottom) in a runaway and a no-reaction response trial, respectively. Looming exposure was paired with LHb inhibition (638 nm, 5 s, 8 mW). At right, the bar graph reports the strategy probability to the looming in the 2 groups (GFP versus Jaws, n_{mice} = 3 versus 3, n_{trials} = 45 versus 45; runaway: 30 versus 10; action-locking: 12 versus 8; no response: 3 versus 27; $X^2_2 = 30$; ***$p < 0.0001$, chi-square test).

Data are presented with boxplots (median and 10th–90th quartile) or means ± SEMs.

See also Figures S2 and S3.

all recorded neurons was significant for each time epoch (Figure 4C). Decoding accuracies showed cluster-specific patterns. Most notably, we found that clusters 3 and 6 showed significant decoding (after correcting for multiple comparison) during the prediction of action epoch, whereas other clusters (including cluster 3) showed significant decoding after the action (Figure 4D). Matching the cluster identity with the topographical neuronal localization during the recordings revealed that the clusters related to prediction, clusters 3 and 6, were located caudally with respect to the rest of the clusters (Figure S4G). Overall, these results demonstrate that distinct neuronal subpopulations within the LHb either predict or reflect defensive behavioral selection in response to a threat.

DISCUSSION

Dissecting the Specific Contribution of LHb Activity for Aversion

In the past decade, we have witnessed a significant growing interest in the essential role the LHb plays in regulating negatively motivated behaviors. LHb neurons at least partly control the function of neuromodulatory systems and are excited by aversive external stimuli (Lecca et al., 2017; Matsumoto and Hikosaka, 2007; Wang et al., 2017). Here, we show that in response to an identical aversive stimulus (an overhead looming), LHb cell dynamics follow opposite logic in a behavior-dependent manner: an escape reaction (runaway) recruits mainly an activation of LHb cells. In contrast, action-locking responses occur along with a decrease in calcium activity, potentially reflecting neuronal inhibition (Namboodiri et al., 2019; Shabel et al., 2019; Wang et al., 2017). Accordingly, aversive foot shock inhibited the neuronal activity of a small and territorially distinct subset of LHb cells (Congiu et al., 2019). Notably, the opposite responses emerging after the looming-driven reaction can occur within the same neuron. It is therefore plausible that a given external stimulus capable of triggering dimorphic reactions drives dissimilar responses in single cells. The substrate (i.e., connectivity or gene) enabling such neuronal populations to encode both behavioral aspects remains an open question.

Functional Heterogeneity in LHb for Threat-Driven Behaviors

Based on recordings and analysis of ~250 LHb cells while animals experience a threat, here, we show how ensembles of neurons represent threat-driven behavioral defensive strategies. An unsupervised clustering reveals that independent sets of active neurons form during the expression of threat-mediated behavioral responses (Gründemann et al., 2019; Namboodiri et al., 2019). Such discrete neuronal clusters are stable and define time frames of threat detection and behavioral action (Gründemann et al., 2019). It remains unclear, however, which neurobiological substrate defines LHb clusters. Within the amygdala and the cortex, genetically distinct neuronal subtypes contribute to different phases of adaptive behaviors (Abs et al., 2018; Douglass et al., 2017; Krabbe et al., 2019). Recent studies identified molecular-level neuronal diversity within the LHb (Hashikawa et al., 2020; Wallace et al., 2020). Exploiting this genetic knowledge may provide an entry point to specifically

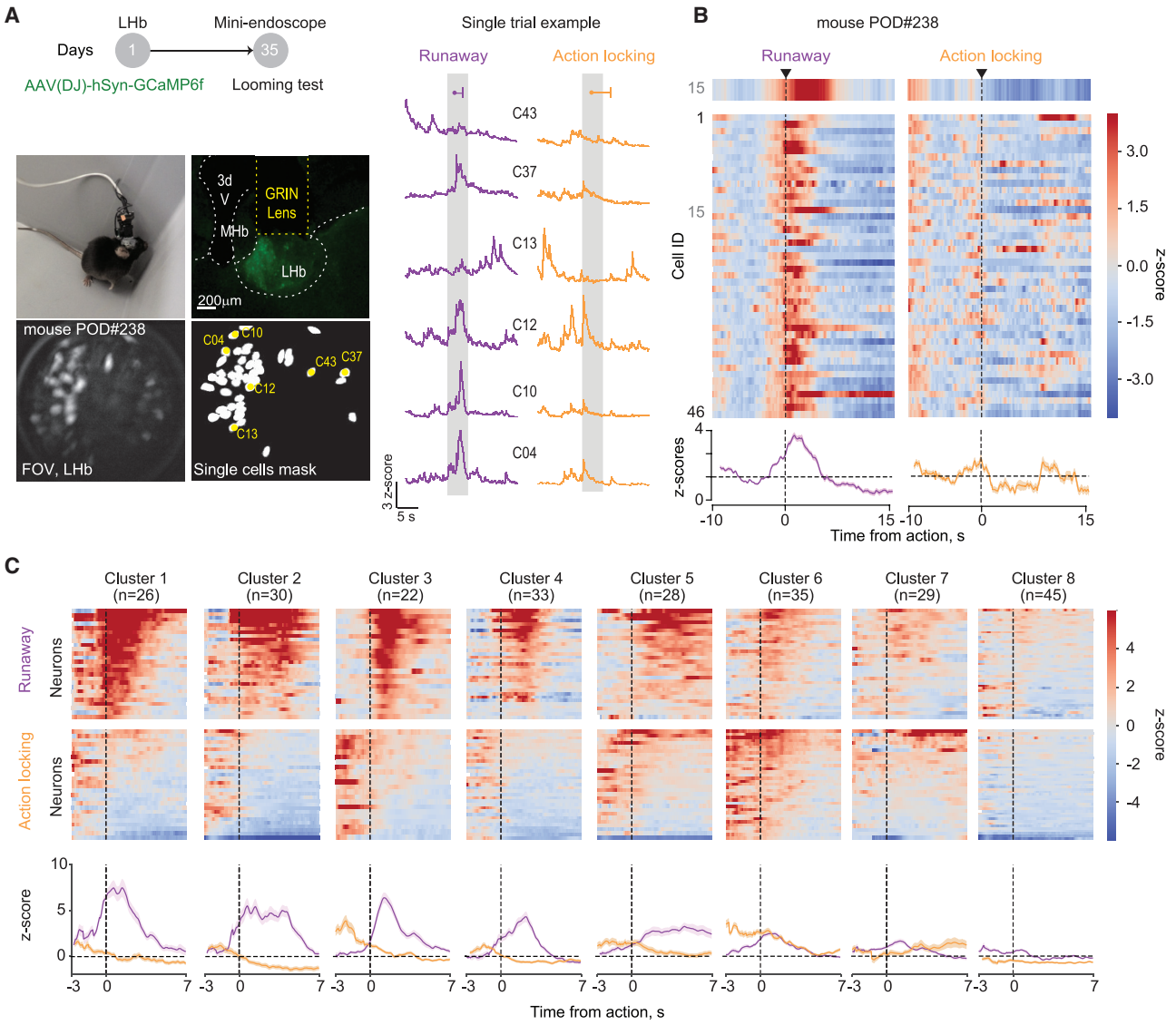

Figure 3. Distinct LHb Neuronal Ensembles during Defensive Behaviors

(A) Top: schematic of the experiment. Bottom, pictures showing mouse with miniscope attached, GRIN lens placement, GCaMP6f expression, field of view with identified cells (maximum intensity projections), map of active LHb neurons, and respective sample traces (right).

(B) Mean Ca^{2+} responses (*Z* score) across runaway (left) and action-locking (right) trials for 46 LHb neurons imaged within a single mouse, aligned to the onset of the behavioral reaction. Highlighted at top, the average response of a single cell (Cell: 15). Bottom, averaged time course of all cells for runaway and action-locking strategies.

(C) Cluster identification by unsupervised classification during runaway (top) and action-locking (center), including all neurons recorded. Bottom, average trace across all of the neurons within the cluster. Plots are aligned to the action onset.

See also Figure S4.

probe the functional and behavioral relevance of individual LHb neuronal clusters identified in this study. As an alternative to a genetic basis, clusters may emerge according to topographical organization, input-specific connectivity, or discrete projection targets (Cerniauskas et al., 2019; Fore and Yaksi, 2019; Shabel et al., 2012; Valentinova et al., 2019). Our analysis indicates that some LHb neuronal clusters are topographically distinct. This heightens the need for future studies to address this unresolved question. Notably, the multilevel heterogeneity (functional, anatomical, and molecular) emerging lately replaces the initial uniform connotation attributed to the LHb. Further studies will need to determine the relationship across these multiple levels of heterogeneity and establish their behavioral relevance.

Complex Neuronal Networks for Defensive Behaviors

The LHb is an evolutionarily conserved structure capable of encoding threats and driving appropriate behaviors in rodents

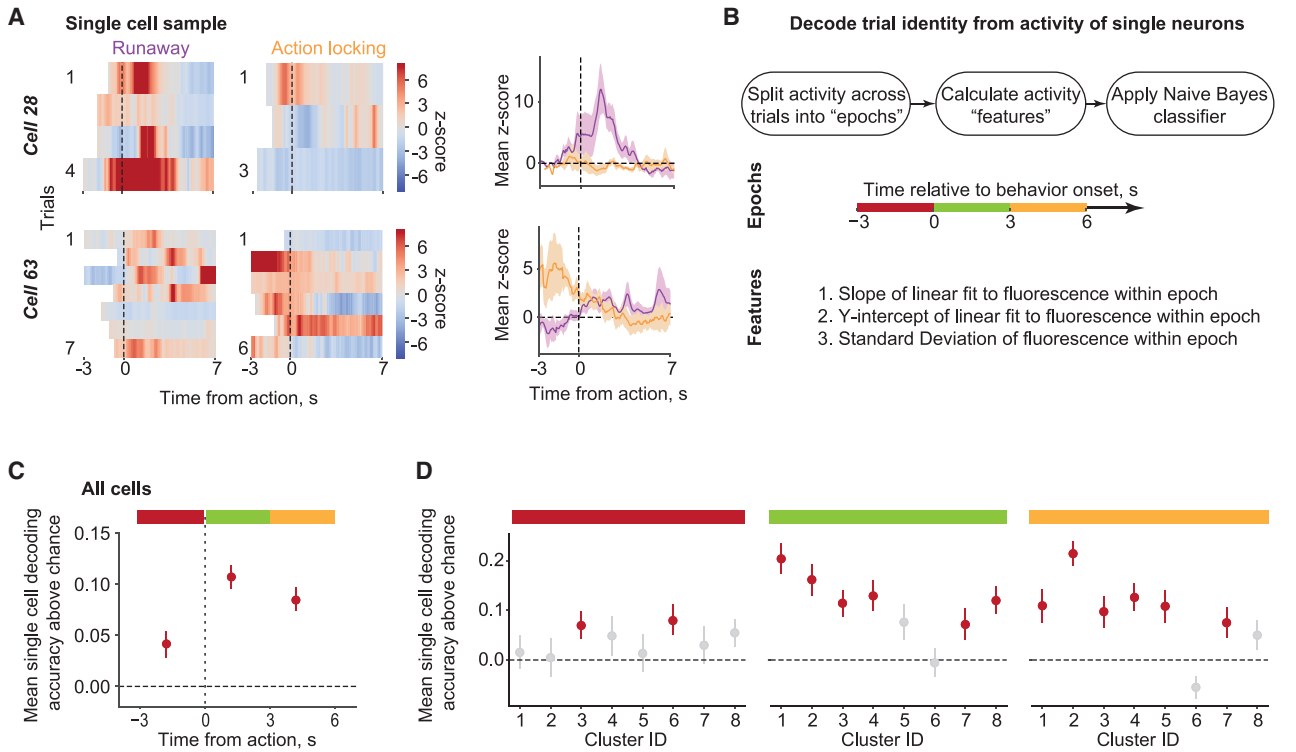

Figure 4. Identified LHb Neuronal Clusters Code for Behavioral Preparation and Execution

(A) Single-cell activity across trials during runaway and action-locking reported as heat plots (left) and mean *Z* score (right). Trials are time-locked with the behavior and presented different onsets due to trial-by-trial variability in reaction time (blank spaces in the heat plots).

(B) Workflow for decoding analysis of single neuron activity. The decoder was run in three different time epochs (−3 to 0 s, burgundy bar; 0–3 s, green bar; 3–6 s, yellow bar) relative to the behavioral onset.

(C) Single-cell decoding accuracy above chance averaged across all recorded neurons. Red dots highlight significance above chance. Error bars reflect SEM. t_{247} = 3.23 for −3 to 0 s, t_{247} = 9.37 for 0–3 s, t_{247} = 7.54 for 3–6 s; p values for the 3 epochs = 2.67×10^{-3}, 1.56×10^{-18}, and 6.84×10^{-13} after Benjamini-Hochberg multiple comparisons correction across all epochs.

(D) Decoding results split by the clusters. Red dots highlight significance above chance. t_{247} = (0.44, 0.12, 2.54, 1.20, 0.35, 2.58, 0.78, and 1.94) for the 8 clusters for −3 to 0 s, t_{247} = (6.62, 5.03, 4.16, 4.20, 2.07, −0.19, 2.25, and 4.33) for the 8 clusters for 0–3 s, t_{247} = (3.13, 8.66, 2.99, 4.43, 3.27, −2.44, 2.42, and 1.67) for the 8 clusters for 3–6 s; p values for the 3 epochs per cluster = (7.55×10^{-1}, 9.07×10^{-1}, 2.99×10^{-2}, 2.96×10^{-1}, 7.97×10^{-1}, 2.63×10^{-2}, 5.28×10^{-1}, and 7.91×10^{-2}) for −3 to 0 s, (2.87×10^{-7}, 4.07×10^{-5}, 5.35×10^{-4}, 3.39×10^{-4}, 6.54×10^{-2}, 4.43×10^{-1}, 4.54×10^{-2}, and 1.89×10^{-4}) for 0–3 s, and (7.78×10^{-3}, 1.18×10^{-10}, 1.12×10^{-2}, 1.89×10^{-4}, 5.67×10^{-3}, 9.84×10^{-1}, 3.22×10^{-2}, and 1.31×10^{-1}) for 3–6 s after Benjamini-Hochberg multiple comparisons correction across all clusters and epochs.

See also Figure S4.

as well as zebrafish (Amo et al., 2014; Fore and Yaksi, 2019; Lecca et al., 2017; Wang et al., 2017). Notably, the initial observation that limiting excitation in LHb impairs looming-driven escape behaviors implicated this structure in the encoding of innate escape (Lecca et al., 2017).

An original aspect of the present work lies in the demonstration that LHb activity changes when animals escape or action-lock after looming presentation. Recent studies support the contribution of several hypothalamic (Daviu et al., 2020; Li et al., 2018), thalamic (Salay et al., 2018; Wei et al., 2015), and midbrain nuclei, mostly for threat-driven escape (Evans et al., 2018; Huang et al., 2017; Seo et al., 2019). Ca^{2+} imaging and brain circuit manipulation approaches demonstrate that glutamatergic neurons of the dorsal periaqueductal gray encode decision making and escape (Evans et al., 2018). In addition, a visual pathway engaging superior colliculus and amygdala also contributes to defensive strategies (Shang et al., 2018). Finally, GABAergic neurons in the ventral tegmental area (VTA) projecting to the central amygdala (CeA) seem to be similarly instrumental in threat-driven escape responses (Zhou et al., 2019). LHb axons innervate these VTA-GABA cells projecting to CeA. Future studies should test how diverse defensive strategies engage wide interconnected network activity to ultimately build an integrated framework for threat-driven behavioral responses. Defensive strategies are a combination of behavioral sets relying on unique features, including trajectories or stereotyped movements (Evans et al., 2019). The use of deep neural network analysis tracking facets of animal behaviors (Nath et al., 2019; Wiltschko et al., 2015) may pave the way to differentiate precise aspects of defensive behaviors. This will allow a refined alignment with the neuronal dynamics in defined neuronal circuits (Klaus et al., 2017).

The unsupervised clustering and decoding analysis provided here support that: (1) LHb activity codes for distinct behavioral

strategies, (2) the dynamics of discrete LHb neuronal clusters reflect precise time epochs of defensive behaviors, and (3) these clusters can predict the upcoming selection of the action or represent an action itself (Grewe et al., 2017; Namboodiri et al., 2019). Broadly perturbing LHb activity during looming presentation reduces runaway responses. This argues for the relevant contribution the LHb may exert on innate behaviors. However, such manipulation of LHb function in a non-cell-specific fashion remains a poor approach to test for causality. Future studies should attempt precise neuronal cluster targeting, a feature highlighted in the functional and topographical analysis provided in this work. This will set the conditions to assess causality between LHb subpopulation activity and defensive strategy. The latest insights of genetic profiling may soon provide the tools to assess these outstanding questions (Hashikawa et al., 2020; Wallace et al., 2020).

In summary, our results identify the evolution of individual neuronal responses in a deep structure like the LHb during threat-driven behavioral strategies, an objective so far proven to be challenging due to technical difficulties. We demonstrated that LHb neuronal clusters participate in the optimal selection of defensive strategies. Future studies can provide a link between this functional heterogeneity with genetic and anatomical aspects to establish a comprehensive knowledge of the contribution of LHb to threat encoding. These findings advance our understanding of the neuronal basis of ethologically relevant innate behaviors.

STAR★METHODS

Detailed methods are provided in the online version of this paper and include the following:

- KEY RESOURCES TABLE
- RESOURCE AVAILABILITY
  - Lead Contact
  - Materials availability
  - Data and Code Availability
- EXPERIMENTAL MODEL AND SUBJECT DETAILS
- METHOD DETAILS
  - Behavioral paradigm
  - Surgical procedures
  - Fiber photometry recordings
  - Endoscope recordings
  - Opto manipulation experiment
- QUANTIFICATION AND STATISTICAL ANALYSIS
  - Analysis
  - Clustering and decoding
  - Statistics

SUPPLEMENTAL INFORMATION

Supplemental Information can be found online at https://doi.org/10.1016/j.celrep.2020.107752.

ACKNOWLEDGMENTS

We thank all of the members of the Mameli laboratory for comments on the manuscript. We thank C. Lüscher, R. Van Zessen, A. Adamantidis, L. Oesch, J. Zapata, and K. Tan for technical assistance. This work was supported by the European Research Council (ERC) StG SalienSy 335333, the Swiss National Funds 31003A and Vaud Canton to M.M., the Brain & Behavior Research Foundation (BBRF) Young Investigator Grant to S.L. and V.M.K.N., and K99MH118422 from the US National Institute of Mental Health to V.M.K.N.

AUTHOR CONTRIBUTIONS

S.L. and M.M. conceptualized the project. S.L. performed and analyzed behaviors and the *in vivo* calcium imaging. L.R. provided support for behavioral analysis and experiments. N.G. performed independent calcium imaging analysis. G.P. provided analytical support for the photometric detection. V.M.K.N. and G.D.S. provided support, analysis for calcium imaging, and help in editing the manuscript. M.M. and S.L. wrote the manuscript with the help of all of the authors.

DECLARATION OF INTERESTS

The authors declare no competing interests.

Received: February 13, 2020
Revised: April 21, 2020
Accepted: May 19, 2020
Published: June 9, 2020

REFERENCES

Abs, E., Poorthuis, R.B., Apelblat, D., Muhammad, K., Pardi, M.B., Enke, L., Kushinsky, D., Pu, D.L., Eizinger, M.F., Conzelmann, K.K., et al. (2018). Learning-Related Plasticity in Dendrite-Targeting Layer 1 Interneurons. Neuron *100*, 684–699.e6.

Amo, R., Fredes, F., Kinoshita, M., Aoki, R., Aizawa, H., Agetsuma, M., Aoki, T., Shiraki, T., Kakinuma, H., Matsuda, M., et al. (2014). The habenulo-raphe serotonergic circuit encodes an aversive expectation value essential for adaptive active avoidance of danger. Neuron *84*, 1034–1048.

Andalman, A.S., Burns, V.M., Lovett-Barron, M., Broxton, M., Poole, B., Yang, S.J., Grosenick, L., Lerner, T.N., Chen, R., Benster, T., et al. (2019). Neuronal Dynamics Regulating Brain and Behavioral State Transitions. Cell *177*, 970–985.e20.

Blanchard, D.C., Canteras, N.S., Markham, C.M., Pentkowski, N.S., and Blanchard, R.J. (2005). Lesions of structures showing FOS expression to cat presentation: effects on responsivity to a Cat, Cat odor, and nonpredator threat. Neurosci. Biobehav. Rev. *29*, 1243–1253.

Blanchard, D.C., Griebel, G., Pobbe, R., and Blanchard, R.J. (2011). Risk assessment as an evolved threat detection and analysis process. Neurosci. Biobehav. Rev. *35*, 991–998.

Cerniauskas, I., Winterer, J., de Jong, J.W., Lukacsovich, D., Yang, H., Khan, F., Peck, J.R., Obayashi, S.K., Lilascharoen, V., Lim, B.K., et al. (2019). Chronic Stress Induces Activity, Synaptic, and Transcriptional Remodeling of the Lateral Habenula Associated with Deficits in Motivated Behaviors. Neuron *104*, 899–915.e8.

Congiu, M., Trusel, M., Pistis, M., Mameli, M., and Lecca, S. (2019). Opposite responses to aversive stimuli in lateral habenula neurons. Eur. J. Neurosci. *50*, 2921–2930.

Cui, G., Jun, S.B., Jin, X., Luo, G., Pham, M.D., Lovinger, D.M., Vogel, S.S., and Costa, R.M. (2014). Deep brain optical measurements of cell type-specific neural activity in behaving mice. Nat. Protoc. *9*, 1213–1228.

Daviu, N., Füzesi, T., Rosenegger, D.G., Rasiah, N.P., Sterley, T.L., Peringod, G., and Bains, J.S. (2020). Paraventricular nucleus CRH neurons encode stress controllability and regulate defensive behavior selection. Nat. Neurosci. *23*, 398–410.

De Franceschi, G., Vivattanasarn, T., Saleem, A.B., and Solomon, S.G. (2016). Vision Guides Selection of Freeze or Flight Defense Strategies in Mice. Curr. Biol. *26*, 2150–2154.

Douglass, A.M., Kucukdereli, H., Ponserre, M., Markovic, M., Gründemann, J., Strobel, C., Alcala Morales, P.L., Conzelmann, K.K., Lüthi, A., and Klein, R. (2017). Central amygdala circuits modulate food consumption through a positive-valence mechanism. Nat. Neurosci. *20*, 1384–1394.

Eilam, D. (2005). Die hard: a blend of freezing and fleeing as a dynamic defense–implications for the control of defensive behavior. Neurosci. Biobehav. Rev. *29*, 1181–1191.

Evans, D.A., Stempel, A.V., Vale, R., Ruehle, S., Lefler, Y., and Branco, T. (2018). A synaptic threshold mechanism for computing escape decisions. Nature *558*, 590–594.

Evans, D.A., Stempel, A.V., Vale, R., and Branco, T. (2019). Cognitive Control of Escape Behaviour. Trends Cogn. Sci. *23*, 334–348.

Fore, S., and Yaksi, E. (2019). Habenula: A Role in Brain State Transitions during Coping Behavior. Curr. Biol. *29*, R692–R694.

Grewe, B.F., Gründemann, J., Kitch, L.J., Lecoq, J.A., Parker, J.G., Marshall, J.D., Larkin, M.C., Jercog, P.E., Grenier, F., Li, J.Z., et al. (2017). Neural ensemble dynamics underlying a long-term associative memory. Nature *543*, 670–675.

Gründemann, J., Bitterman, Y., Lu, T., Krabbe, S., Grewe, B.F., Schnitzer, M.J., and Lüthi, A. (2019). Amygdala ensembles encode behavioral states. Science *364*, eaav8736.

Hashikawa, Y., Hashikawa, K., Rossi, M.A., Basiri, M.L., Liu, Y., Johnston, N.L., Ahmad, O.R., and Stuber, G.D. (2020). Transcriptional and Spatial Resolution of Cell Types in the Mammalian Habenula. Neuron. https://doi.org/10.1016/j.neuron.2020.03.011.

Headley, D.B., Kanta, V., Kyriazi, P., and Paré, D. (2019). Embracing Complexity in Defensive Networks. Neuron *103*, 189–201.

Huang, L., Yuan, T., Tan, M., Xi, Y., Hu, Y., Tao, Q., Zhao, Z., Zheng, J., Han, Y., Xu, F., et al. (2017). A retinoraphe projection regulates serotonergic activity and looming-evoked defensive behaviour. Nat. Commun. *8*, 14908.

Klaus, A., Martins, G.J., Paixao, V.B., Zhou, P., Paninski, L., and Costa, R.M. (2017). The Spatiotemporal Organization of the Striatum Encodes Action Space. Neuron *96*, 949.

Krabbe, S., Paradiso, E., d'Aquin, S., Bitterman, Y., Courtin, J., Xu, C., Yonehara, K., Markovic, M., Müller, C., Eichlisberger, T., et al. (2019). Adaptive disinhibitory gating by VIP interneurons permits associative learning. Nat. Neurosci. *22*, 1834–1843.

Lazaridis, I., Tzortzi, O., Weglage, M., Märtin, A., Xuan, Y., Parent, M., Johansson, Y., Fuzik, J., Fürth, D., Fenno, L.E., et al. (2019). A hypothalamus-habenula circuit controls aversion. Mol. Psychiatry *24*, 1351–1368.

Lecca, S., Meye, F.J., Trusel, M., Tchenio, A., Harris, J., Schwarz, M.K., Burdakov, D., Georges, F., and Mameli, M. (2017). Aversive stimuli drive hypothalamus-to-habenula excitation to promote escape behavior. eLife *6*, e30697.

Li, Y., Zeng, J., Zhang, J., Yue, C., Zhong, W., Liu, Z., Feng, Q., and Luo, M. (2018). Hypothalamic Circuits for Predation and Evasion. Neuron *97*, 911–924.e5.

Matsumoto, M., and Hikosaka, O. (2007). Lateral habenula as a source of negative reward signals in dopamine neurons. Nature *447*, 1111–1115.

Namboodiri, V.M.K., Otis, J.M., van Heeswijk, K., Voets, E.S., Alghorazi, R.A., Rodriguez-Romaguera, J., Mihalas, S., and Stuber, G.D. (2019). Single-cell activity tracking reveals that orbitofrontal neurons acquire and maintain a long-term memory to guide behavioral adaptation. Nat. Neurosci. *22*, 1110–1121.

Nath, T., Mathis, A., Chen, A.C., Patel, A., Bethge, M., and Mathis, M.W. (2019). Using DeepLabCut for 3D markerless pose estimation across species and behaviors. Nat. Protoc. *14*, 2152–2176.

Resendez, S.L., Jennings, J.H., Ung, R.L., Namboodiri, V.M., Zhou, Z.C., Otis, J.M., Nomura, H., McHenry, J.A., Kosyk, O., and Stuber, G.D. (2016). Visualization of cortical, subcortical and deep brain neural circuit dynamics during naturalistic mammalian behavior with head-mounted microscopes and chronically implanted lenses. Nat. Protoc. *11*, 566–597.

Salay, L.D., Ishiko, N., and Huberman, A.D. (2018). A midline thalamic circuit determines reactions to visual threat. Nature *557*, 183–189.

Seo, C., Guru, A., Jin, M., Ito, B., Sleezer, B.J., Ho, Y.Y., Wang, E., Boada, C., Krupa, N.A., Kullakanda, D.S., et al. (2019). Intense threat switches dorsal raphe serotonin neurons to a paradoxical operational mode. Science *363*, 538–542.

Shabel, S.J., Proulx, C.D., Trias, A., Murphy, R.T., and Malinow, R. (2012). Input to the lateral habenula from the basal ganglia is excitatory, aversive, and suppressed by serotonin. Neuron *74*, 475–481.

Shabel, S.J., Wang, C., Monk, B., Aronson, S., and Malinow, R. (2019). Stress transforms lateral habenula reward responses into punishment signals. Proc. Natl. Acad. Sci. USA *116*, 12488–12493.

Shang, C., Chen, Z., Liu, A., Li, Y., Zhang, J., Qu, B., Yan, F., Zhang, Y., Liu, W., Liu, Z., et al. (2018). Divergent midbrain circuits orchestrate escape and freezing responses to looming stimuli in mice. Nat. Commun. *9*, 1232.

Silva, B.A., Mattucci, C., Krzywkowski, P., Cuozzo, R., Carbonari, L., and Gross, C.T. (2016). The ventromedial hypothalamus mediates predator fear memory. Eur. J. Neurosci. *43*, 1431–1439.

Tovote, P., Esposito, M.S., Botta, P., Chaudun, F., Fadok, J.P., Markovic, M., Wolff, S.B., Ramakrishnan, C., Fenno, L., Deisseroth, K., et al. (2016). Midbrain circuits for defensive behaviour. Nature *534*, 206–212.

Trusel, M., Nuno-Perez, A., Lecca, S., Harada, H., Lalive, A.L., Congiu, M., Takemoto, K., Takahashi, T., Ferraguti, F., and Mameli, M. (2019). Punishment-Predictive Cues Guide Avoidance through Potentiation of Hypothalamus-to-Habenula Synapses. Neuron *102*, 120–127.e4.

Valentinova, K., Tchenio, A., Trusel, M., Clerke, J.A., Lalive, A.L., Tzanoulinou, S., Matera, A., Moutkine, I., Maroteaux, L., Paolicelli, R.C., et al. (2019). Morphine withdrawal recruits lateral habenula cytokine signaling to reduce synaptic excitation and sociability. Nat. Neurosci. *22*, 1053–1056.

Wallace, M.L., Huang, K.W., Hochbaum, D., Hyun, M., Radeljic, G., and Sabatini, B.L. (2020). Anatomical and single-cell transcriptional profiling of the murine habenular complex. eLife *9*, e51271.

Wang, D., Li, Y., Feng, Q., Guo, Q., Zhou, J., and Luo, M. (2017). Learning shapes the aversion and reward responses of lateral habenula neurons. eLife *6*, e23045.

Wei, P., Liu, N., Zhang, Z., Liu, X., Tang, Y., He, X., Wu, B., Zhou, Z., Liu, Y., Li, J., et al. (2015). Processing of visually evoked innate fear by a non-canonical thalamic pathway. Nat. Commun. *6*, 6756.

Wiltschko, A.B., Johnson, M.J., Iurilli, G., Peterson, R.E., Katon, J.M., Pashkovski, S.L., Abraira, V.E., Adams, R.P., and Datta, S.R. (2015). Mapping Sub-Second Structure in Mouse Behavior. Neuron *88*, 1121–1135.

Yilmaz, M., and Meister, M. (2013). Rapid innate defensive responses of mice to looming visual stimuli. Curr. Biol. *23*, 2011–2015.

Zhou, Z., Liu, X., Chen, S., Zhang, Z., Liu, Y., Montardy, Q., Tang, Y., Wei, P., Liu, N., Li, L., et al. (2019). A VTA GABAergic Neural Circuit Mediates Visually Evoked Innate Defensive Responses. Neuron *103*, 473–488.e6.

Zhou, P., Resendez, S.L., Rodriguez-Romaguera, J., Jimenez, J.C., Neufeld, S.Q., Giovannucci, A., Friedrich, J., Pnevmatikakis, E.A., Stuber, G.D., Hen, R., et al. (2018). Efficient and accurate extraction of in vivo calcium signals from microendoscopic video data. Elife *7*, e28728.

STAR★METHODS

KEY RESOURCES TABLE

REAGENT or RESOURCE	SOURCE	IDENTIFIER
Experimental models		
C57BL6J	Janvier Laboratories France	N/A
Bacterial and Virus Strains		
rAAV2.1-hSyn-GCaMP6f-	University of North Carolina Viral vector core	N/A
rAAV/DJ-hSyn- -GCaMP6f	University of North Carolina Viral vector core	N/A
rAAV2.5-hSyn-eGFP	University of North Carolina Viral vector core	N/A
rAAV5-hSyn-JAWS-eGFP	Trusel et al., 2019	Addgene, Cat#65014 AAV5
Software and Algorithms		
Spike2	Lecca et al., 2017	http://ced.co.uk/products/spkovin
nVista	Resendez et al., 2016	https://www.inscopix.com
Mosaic, EDPS	Inscopix	https://www.inscopix.com
CNMF-E	Zhou et al., 2018	https://www.github.com/zhoupc/cnmf_e)
Cluster algorithm	Namboodiri et al., 2019	N/A

RESOURCE AVAILABILITY

Lead Contact

Further information and requests for resources and reagents should be directed to and will be fulfilled by the Lead Contacts, Manuel Mameli (manuel.mameli@unil.ch)

Materials availability

This study did not generate new unique reagents.

Data and Code Availability

The dataset and code supporting the current study have not been yet deposited in a public repository. This process is ongoing through discussion with the main Institution. Nevertheless, the entire dataset is available from the corresponding author on request.

EXPERIMENTAL MODEL AND SUBJECT DETAILS

The experiments were performed on C57BL/6J mice wild-type males and females of 10-18 weeks. Mice were housed at groups of five per cage with water and food *ad libitum* on a 12:12 h light cycle (lights on at 7 a.m.). All procedures aimed to fulfill the 3R criterion and were approved by the Veterinary Offices of Vaud (Switzerland; License VD3171).

METHOD DETAILS

Behavioral paradigm

Mice were tested for behavior in a looming visual stimulus test, as described elsewhere (Yilmaz and Meister, 2013). Animals were placed in an open-top plexiglas box (58cm L × 38cm W × 32cm H). A triangular shaped nest (20 × 12 cm) was placed in one corner. Recordings were performed under illumination provided by the projector screen (52 cm × 30 cm; Dell) and an infrared light-emitting diode (LED) illuminator (Pinnacle Technology), both placed above the arena. In a separate set of experiments, the projector screen was placed inside the arena in a side (the far side respect to the nest) to provide the same looming stimulus from a frontal (non-threatening) perspective (Zhou et al., 2019). Experiments were recorded at 60 frames per second with a near-IR GigE camera (acA1300-60 gmNIR, Basler) positioned in one side of the arena. Video recording, was controlled with Ethovision and synchronized with the photometric and endoscopic recordings using hardware-time signals controlled with a I/O box (Noldus). All the mice tested underwent a period of habituation to the fiber/camera spanning from 15-20 min session every day for 3 consecutive days. For the experiment, after 5-10 min of acclimatization, a visual stimulus (always delivered at 50% contrast), was randomly presented from the screen in the center of the arena while the mouse was actively exploring (independently by its position in the arena). A single stimulus consists

in the repetition of 5 looming (single looming duration 0.5 s, inter-looming interval 0.5 s) (Evans et al., 2018). Each mouse received from 7 to 20 trials with a minimum inter-trial interval of about 5 minutes. The video analysis of the behavior was performed offline.

Automated detection of mouse shape and position

A fully convolutional neural network was used to extract the shape of the mouse across the arena. Each video (1920 × 1088 @ 60 fps) was converted to a sequence of images (8-bit, 256 × 144 pixel). The training dataset was composed of 112 images and it was used to trace a set of 112 masks (8-bit, 256 × 144 pixel binary images) delineating the contour of the mouse body and to output the files storing the coordinates of the center of mass of each individual mask. Each image in the training dataset was passed through three convolutional layers (channels: 16, 32, 64; kernels: 3, 5, 3, stride: 1, ReLU units), two max-pooling operations (kernel size: 2), and three transposed convolutional layers. The frames were processed in batches of 64 images for 171 epochs). The network was built with the open source library PyTorch 1.2 (https://pytorch.org/) and trained to minimize (Adam optimizer, learning rate: 0.003) the Mean-Squared Error loss function. Accuracy was measured as the Euclidean distance between the centroid of the mask of the training set and the centroid of the score map predicted by the network. An arbitrary cutoff was used to define the boundaries of the estimated mouse shape on the score map. The mean accuracy on the test set was 1.65 px (+/− 1.51 px, standard deviation), with 96.4% of the frames showing a distance between centroids (i.e., label Vs predicted) less than 7 px. The output coordinates of the center of mass were then used to compute the speed (pixels/seconds) and the location of the mouse inside the arena. The onset of runaway was measured as the peak of the first derivative of the mouse speed tracking curve. The runaway offset was coinciding with the mouse entrance in the nest. The score map was used to estimate the size of the mouse (e.g., total number of pixel above the arbitrary threshold) across the arena and used for further calculations to score action-locking behavior.

Automated classification of action-locking behavior

An observer blind to the experimental condition of the animals manually scored the action locking behavior, defined as a sudden blockade of all -except respiratory- movements. In contrast to freezing, action locking was not associated with a particular body posture (i.e., crouching). The sudden immobility had to last at least two seconds in order to score the animal as actively producing an action-locking behavior. Data obtained from the manually labeled frames were then merged with the data (speed and size) obtained from the automatic detection of the mouse position to train a random forest classifier to predict in each frame whether the animal was in action-locking. Both speed and size were convolved with a Max function (window = 60 frames) and a total of four features were used: speed (v), size (s), es, and ev. A 5-fold cross-validation yielded an overall accuracy of 98%. The accuracy achieved on the test set was 97.5% with a false positive rate of 2.6%.

Surgical procedures

Viral injections

All mice were anaesthetized with ketamine (150 mg/kg)/xylazine (10 mg/kg) (Sigma-Aldrich, France). We unilaterally injected in the LHb (−1.4 mm AP, 0.45 ML, 3.1 mm DV) rAAV2.1-hSyn-GCaMP6f- or rAAV/DJ-hSyn- -GCaMP6f- or rAAV2.5-hSyn-eGFP (University of North Carolina, US) using a glass pipette on a stereotactic frame (Kopf, France). For optogenetic experiments, we bilaterally injected in the LHb the inhibitory opsin rAAV5-hSyn-JAWS-eGFP (Addgene, US) or rAAV2.5-hSyn-eGFP. Volumes ranged between 200 and 300 nl, at a rate of approximately 100-150 nl/min. The injection pipette was withdrawn from the brain 10 minutes after the infusion. Animals were allowed to recover for a minimum of two weeks before fiber or GRIN lenses implantation.

Chronic implants

For fiber photometry experiments, a single fiber probe (200 μm, Chi Square Bioimaging) was placed and fixed (C and B Metabond, Parkell) 150 μm above the injection site. For optogenetic manipulation a single fiber (200 μm, Thorlabs) was placed at the following coordinates from Bregma (AP: −1.4 mm, L: ± 0.1 mm, V: −2.6 mm from skull surface). Surgery was performed under isoflurane anesthesia (induction: 4%, maintenance: 1.8%–2%).

For endoscope experiments, mice were anaesthetized (as described above) and implanted with a GRIN (Graded-Index) lens (6.1mm length, 0.5mm diameter; Inscopix, #100-000588). The lens was targeted to be ∼150–200 μm above the injection site using the following coordinates: −1.40 mm posterior to bregma, 0.45 mm lateral from midline, and −2.85 to −2.9 mm ventral to skull surface (lowered at a speed of 1μm/s). To increase stability of the implants the lenses were implanted into the dorsal portion of the region allowing imaging ventral LHb neurons. Two week after lens implantation, mice were again anaesthetized (isoflurane, as above) and a baseplate (Inscopix, #100- 000279) was secured above the lens. A baseplate cover (Inscopix, #100-000241) was attached to prevent damage to the microendoscope lens. Out of 23 mice that were injected with GCaMP6f virus, 4 had successful lens implantation/viral expression and were used for this study.

Fiber photometry recordings

Fiber photometry measurements were carried out by the ChiSquare X2-200 system (ChiSquare Biomaging, Brookline, MA). Briefly, blue light from a 473-nm picosecond-pulsed laser (at 50 MHz; pulse width ∼80 ps FWHM) was delivered to the sample through a single mode fiber. Fluorescence emission from the tissue was collected by a multimode fiber with a sample frequency of 100Hz. The single mode and multimode fibers were arranged side by side in a ferrule that is connected to a detachable multimode fiber implant. The emitted photons collected through the multimode fiber pass through a bandpass filter (FF01-550/88, Semrock) to a single-photon detector. Photons were recorded by the time-correlated single photon counting (TCSPC) module (SPC-130EM, Becker and Hickl, GmbH, Berlin, Germany) in the ChiSquare X^2-200 system.

Endoscope recordings

All calcium imaging was recorded at 20 frames per second, 200-ms exposure time, and 10%–40% LED power (0.4-0.9mW at the objective, 475nm) using a miniature microscope from Inscopix (nVista). Calcium recording files were down-sampled (spatial binning factor of 4) to reduce processing time and file size, filtered, corrected for rigid brain movement and the ΔF/F0 was calculated using as F0 the average fluorescence for all the video (Inscopix, IDP). Individual component analysis and principle component analysis (ICA/PCA) applications were used to identify individual cells and to extract their respective calcium traces.

In addition, to compare ROI detections and relative traces obtained with the PCA/ICA we also performed constrained non-negative matrix factorization for endoscopic data (CNMF-E) for a subset of data. Briefly, we denoised, deconvolved, and demixed calcium-imaging dynamics (https://www.github.com/zhoupc/cnmf_e). This method allows accurate single neurons fluorescence traces extraction (Zhou et al., 2018). Calcium imaging frames were initially pre-processed in Mosaic (Inscopix) for motion correction. We use a Gaussian kernel width 4 μm, maximum soma diameter 16 μm, minimum local correlation 0.8, minimum peak-to-noise ratio 8 and merging threshold was set to 0.65 for optimal discrimination of temporal and spatial overlap.

Opto manipulation experiment

For experiments employing JAWS *in vivo*, light was provided through a laser-coupled fiber optic at 638 nm (MatchBox series, Integrated Optics, US). Light was applied during the entire presentation of the stimulus (5 s) at a power of 8 mW at the tip of the fiber.

In vivo *recordings*

For the JAWS validation *in vivo*, mice were previously injected unilaterally in the LHb with rAAV2-hSyn-JAWS-eGFP. During the recordings mice were anesthetized using isoflurane (Univentor, Malta. Induction: 2%; maintenance: 1%–1.5%) and placed in the stereotaxic apparatus (Kopf, Germany). Their body temperature was maintained at 36 ± 1C using a feedback-controlled heating pad (CMA 450 Temperature controller, USA). An optrode was lowered at the coordinates of LHb to isolate single-cell spiking. Recordings were performed in both hemisphere (infected versus not infected). For each cell encountered we recorded a 2-3 minutes' stable baseline and we tested its response to a single light pulse (638nm, 8mW, 10 s). Peri-stimulus time histograms (PSTHs) and raster plots were built from 10 to 15 stimulus repetitions and displayed using 1 s bin width.

QUANTIFICATION AND STATISTICAL ANALYSIS

Analysis

Photometric signal as well as miniscope ICA/PCA derived traces were smoothed (constant time factor, 0.1 s) and further processed according to the trials using Spike2 software (Cambridge Electronic Design). We obtained an average peri-stimulus time histogram (PSTH) trace aligned to the stimulus or behavioral onset/offset (3 s prior and 7 s after a given event). For all the recordings we z-scored each trials in reference to their baseline (3 s prior to the looming onset).

For the comparison between speed and photon change (Figure S2), we selected the first runaway and action locking response for each mouse. Then we looked for a single episode outside looming presentation with a comparable change in speed for the same mouse. The change in speed was calculated subtracting the peak/dip speed from the baseline speed (3 s prior). With the same logic we extracted the relative photon change. To further analyze whether LHb activity was influenced by spontaneous locomotion, in mini-endoscope implanted mice, we selected episodes of start/stop movement (5 to 10 episodes outside looming per mouse; 4 s width, 2 s offset) and we reported the relative averaged single cell activity (z-scored using the offset as baseline reference; Figure S4).

We identified functional sub-classes of neurons (Figure S4) by comparing the fluorescence Ca^{2+} signals of individual cells before and after a given event, using 2 s time span. For runaway trials we consider a cell excited if the signal 2 s post runaway onset was higher than the baseline plus 2 SD. Vice versa a cell was inhibited if its signal in the 2 s post runaway resulted 2 SD lower than their baseline. For action-locking responses we considered 3 epochs (2 s each epoch) of analysis post event according with the average duration of this behavior (6 s). If the signal in at least one epoch resulted higher or lower than 2 SD of the baseline the cell was considered action-locking excited or inhibited respectively.

For the analysis of the single trials we follow the same logic above-mentioned except that the epochs considered for the action locking were updated each time according with the duration of the response.

Clustering and decoding

For clustering neurons based on their average responses around action onset for both action-locking and runaway trials, we followed a similar general procedure as in Namboodiri et al. (2019). Briefly, we first calculated the average peri-event time histogram (PETH) for each neuron around each action by averaging all trials. Due to the variability in reaction times from looming stimulus onset until the action, we calculated the PETHs around a time window from −0.5 s to +7 s surrounding the action. This ensured that only activity after the looming stimulus onset was included in all trials. The PETH surrounding both action-locking and runaway trials were treated as features of the response of a neuron. This feature space was then reduced in dimensionality using principal components analysis. The number of principal components to keep was decided based on the bend in the scree plot (Namboodiri et al., 2019). A spectral clustering algorithm along with optimal selection of number of clusters using silhouette scores (Namboodiri et al., 2019) was used on the principal component scores to test for presence of clusters. The number of clusters was chosen by maximizing the silhouette score. Once cluster identities were assigned, all PETHs were recalculated using the activity from −3 s to +7 s surrounding

the actions. Only activity following looming stimulus onset was included. If the looming stimulus onset was less than 3 s prior to action on a trial, these data were treated as "not a number (nan)" in our analysis pipeline.

We then tested for significant decoding by analyzing whether the activity of a single neuron could be used to decode the chosen behavioral action on a trial.

To calculate a decoding accuracy, we trained a Naive Bayes classifier on all but one trial (leave-one-out cross-validation) and tested the decoding accuracy on the remaining trial for each time epoch (Figure 4B). Within each epoch, three "response features" were used for decoding analysis: slope of the linear fit to fluorescence within the epoch, y-intercept of this fit, and lastly, the standard deviation of fluorescence within the epoch (Figure 4B). Only three features were used to avoid overfitting and maximize generalizability of decoding on test trials. The accuracy for a single test trial was defined as 1 if the trial was correctly classified and 0 if it was incorrectly classified. This procedure was repeated with each trial as a test trial (and the remaining as training trials) to obtain a mean cross-validated accuracy. We then calculated a mean accuracy expected by chance by shuffling trial identity. This procedure was repeated with each trial as the test trial, to obtain an overall decoding accuracy above chance accuracy obtained by shuffling trial identity. For the shuffled null, we calculated the mean chance accuracy per neuron as the mean accuracy across ten different shuffles. We applied this procedure to one neuron at a time to obtain a decoding accuracy per neuron, which was then averaged across all neurons recorded, or all neurons within a cluster. The decoding accuracy above chance was simply calculated as the difference in population mean between the true accuracies and the shuffled accuracies. Significance was tested based on a two-sample t test between the true accuracies and the shuffled accuracies.

Statistics

Offline analyses were performed using Prism 8 (Graphpad, US). Single data points are always plotted. Sample size was pre-estimated from previously published research and from pilot experiments performed in the laboratory. Each mouse represents an analytical unit, for each experiment we stated the replication factor. The Area Under Curve (AUC) was calculated for each trial considering all the curve reported in the relative figure. Compiled data are expressed as boxplots (median and quartiles) or mean ± SEM. Significance was set at $p < 0.05$ using two-sided unpaired t test, one or two-way ANOVA. Correlational analysis was performed with Pearson test. Frequency distribution was analyzed with X^2 test. The use of the paired t test, one way and two way ANOVA for repeated-measured as well as the Dunnett's multiple comparisons test were stated in the legend figure text.

Cell Reports, Volume *31*

Supplemental Information

Heterogeneous Habenular Neuronal Ensembles during Selection of Defensive Behaviors

Salvatore Lecca, Vijay M.K. Namboodiri, Leonardo Restivo, Nicolas Gervasi, Giuliano Pillolla, Garret D. Stuber, and Manuel Mameli

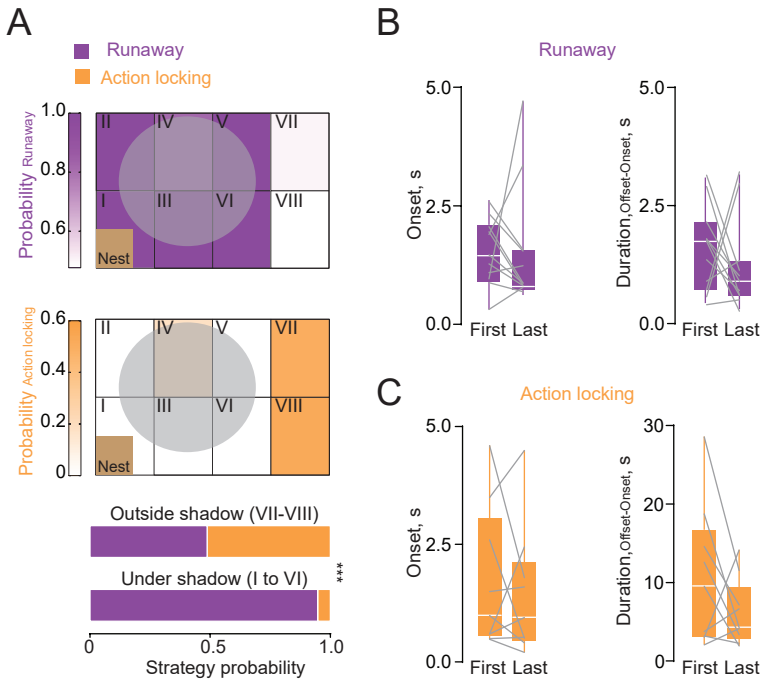

Figure S1. Shadow projection modulate runaway and action locking responses that are stable in time, Related to Figure 1.
(A) Top: Arena representation divided in zones (from I to VIII) reporting the max loom shadow projection and the probability (heat-plots) for runaway (R) and action locking (AL) responses plotted in each zone (n_{mice}=11; $n_{runaway}$= 56; Zone = trials; I = 2, II = 5, III = 5, IV = 9, V = 8, VI = 7, VII = 10, VIII = 10. $n_{action\ locking}$= 23; I = 0, II = 0, III = 0, IV = 2, V = 0, VI = 0, VII = 11, VIII = 10). Bottom. Bar graph reporting the probability of R and AL respect to the max looming shadow projection (R vs AL, Outside shadow, zone VII and VIII: 20 vs 21; Under shadow, zone I to VI: 36 vs 2; $X^2_1 = 20.18$; ***p<0.0001, Chi Square test).
(B) Reaction onset (n_{mice}= 11, first vs last trial; 1.52 ± 0.22 s vs 1.56 ± 0.43 s; t_{10}=0.094, p=0.93, paired t-test) and duration (first vs last trial; 1.58 ± 0.27 s vs 1.2 ± 0.29 s; t_{10}= 0.794, p=0.44, paired t-test) for the first and last Runaway response for each mouse.
(C) Same as (B) but for Action-locking trials (n_{mice}=9, first vs last trial; Onset: 1.71 ± 0.50 s vs 1.44 ± 0.46 s; t_8= 0.561, p=0.59, paired t-test. Duration: 10.72 ± 2.98 s vs 6.2 ± 1.4 s; t_8=1.50, p=0.17, paired t-test).

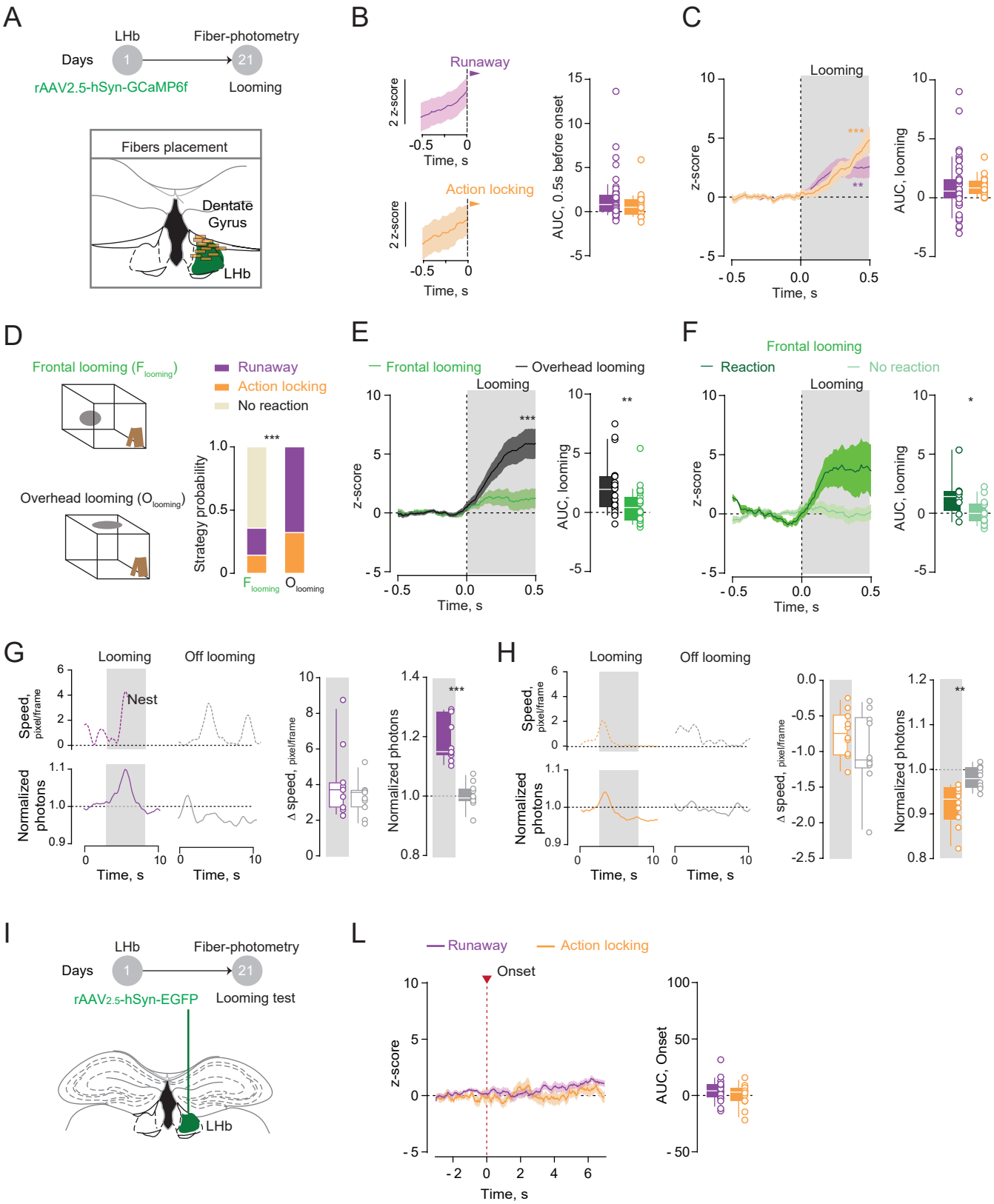
A
LHb
Fiber-photometry
Days
1
21
rAAV2.5-hSyn-GCaMP6f
Looming
Fibers placement
Dentate Gyrus
LHb
B
Runaway
2 z-score
-0.5
0
Time, s
Action locking
AUC, 0.5s before onset
C
Looming
z-score
***
**
AUC, looming
D
Frontal looming (F looming)
Overhead looming (O looming)
Runaway
Action locking
No reaction
Strategy probability
E
Frontal looming
Overhead looming
F
Reaction
No reaction
G
Looming
Off looming
Nest
Speed, pixel/frame
Normalized photons
Δ speed, pixel/frame
H
I
rAAV2.5-hSyn-EGFP
Looming test
L
Onset
AUC, Onset

Figure S2. Looming-driven Ca2+ dynamics within the LHb are threat dependent but independent of locomotion, Related to Figure 2.

(A) Schematic of fiber placement in the LHb (brown rectangles represent fiber tip placement)

(B) Averaged traces and boxplots for Runaway (R, 56 trials) and Action locking (AL, 23 trials) reporting the AUC 0.5 s before the behavioral onset (R vs AL, 1.45 ± 0.31 vs 0.75 ± 0.30, t_{77}= 1.348, p= 0.182 Unpaired t-test)

(C) z-scored traces and area under curve (AUC) showing the LHb activity time-locked with the looming onset for Runaway (51 trials, F_{2550}= 5.79; **p=0.008, RM One way ANOVA) and Action locking trials (18 trials, F_{867}= 10.12; ***p=0.0003, RM One way ANOVA). Boxplots reported the AUC for the same set of data (R vs AL, 0.94 ± 0.30 vs 0.97± 0.20; t_{67}= 0.066, p=0.94 Unpaired t-test).

(D) Left. Representative drawings illustrating the arena setting for the frontal looming (top, $F_{looming}$) and the classical overhead looming (bottom, $O_{looming}$). Right. Bar graph reporting the probability of Runaway (R), Action locking (AL) or no reaction (NR) in response to the frontal or overhead looming (n_{mice}= 5; $F_{looming}$: $n_{runaway}$= 6, $n_{action\ locking}$= 4, $n_{no\ reaction}$= 18. $O_{looming}$: $n_{runaway}$= 19, $n_{action\ locking}$= 9, $n_{no\ reaction}$= 0. X^2_2= 26.68; ***p<0.0001, Chi Square test).

(E) z-scored traces and AUC showing the LHb activity time-locked with the looming for the $F_{looming}$ (26 trials, F_{1250}= 0.671; p=0.502, RM One way ANOVA) and the $O_{looming}$ (25 trials, F_{2250}= 10.15; ***p=0.0005, RM One way ANOVA). Boxplots reported the AUC for the same set of data ($F_{looming}$ vs $O_{looming}$, 0.53 ± 0.27 vs 1.97± 0.42; t_{49}= 2.87, **p=0.0061 Unpaired t-test).

(F) Same as (E) but only for the $F_{looming}$ trials divided in trials triggering a reaction (R or AL) and trials were the mouse do not react (Reaction vs No reaction, 8 vs 18 trials; 1.49 ± 0.64 vs 0.10 ± 0.23; t_{24}= 2.54, *p=0.017, Unpaired t-test)

Note that for this analysis trials displaying a behavioral onset < 0.5 sec were discarded to avoid behavior-dependent signal contamination.

(G) Representative traces and boxplots reporting increase in speed (Looming on vs Looming off; 11 vs 11; 4.1 ± 0.56 vs 3.3 ± 0.28 pixel/frame; t_{20}=1.28, p=0.21 Unpaired t-test) and the relative LHb activity (Looming on vs Looming off; 11 vs 11, 1.19±0.02 vs 1.00 ± 0.012 normalized photon; t_{20} = 7.35, ***p<0.0001 Unpaired t-test) in presence or absence of the looming stimulus.

(H) Same as (G) but for decrease in speed (Looming on vs Looming off; 10 vs 10; -0.7558 ± 0.10 vs -0.9987 ± 0.176 pixel/frame; t_{18}=1.190, p=0.249 Unpaired t-test) and relative LHb photon change (Looming on vs Looming off; 10 vs 10, 0.9204±0.014 vs 0.9807±0.007 normalized photons; t_{18}=3.61, **p=0.002 Unpaired t-test).

For this comparison, we selected the first runaway and action locking response for each mouse. Then we looked for a single episode outside looming presentation with a comparable change in speed for the same mouse. Note that one mouse did not display any action locking response throughout the recording session.

(I) Schematic of the experiment and representative brain coronal section showing eGFP injections in the LHb (n_{mice}= 5).

(L) Left: z-score time-course graph showing averaged traces of Runaway (R, n_{trials}= 21, F_{1400}=2, p=0.074 RM One way ANOVA) and Action-locking (AL, n_{trials}= 12, F_{770}=3.347, p=0.269 RM One way ANOVA) trials time-locked with the behavioral onset. Right: area under curve (AUC) for the same data set (R vs AL, 4.87 ± 2.12 vs 0.191 ± 2.96 t31=1.303, p=0.202, Unpaired t-test).

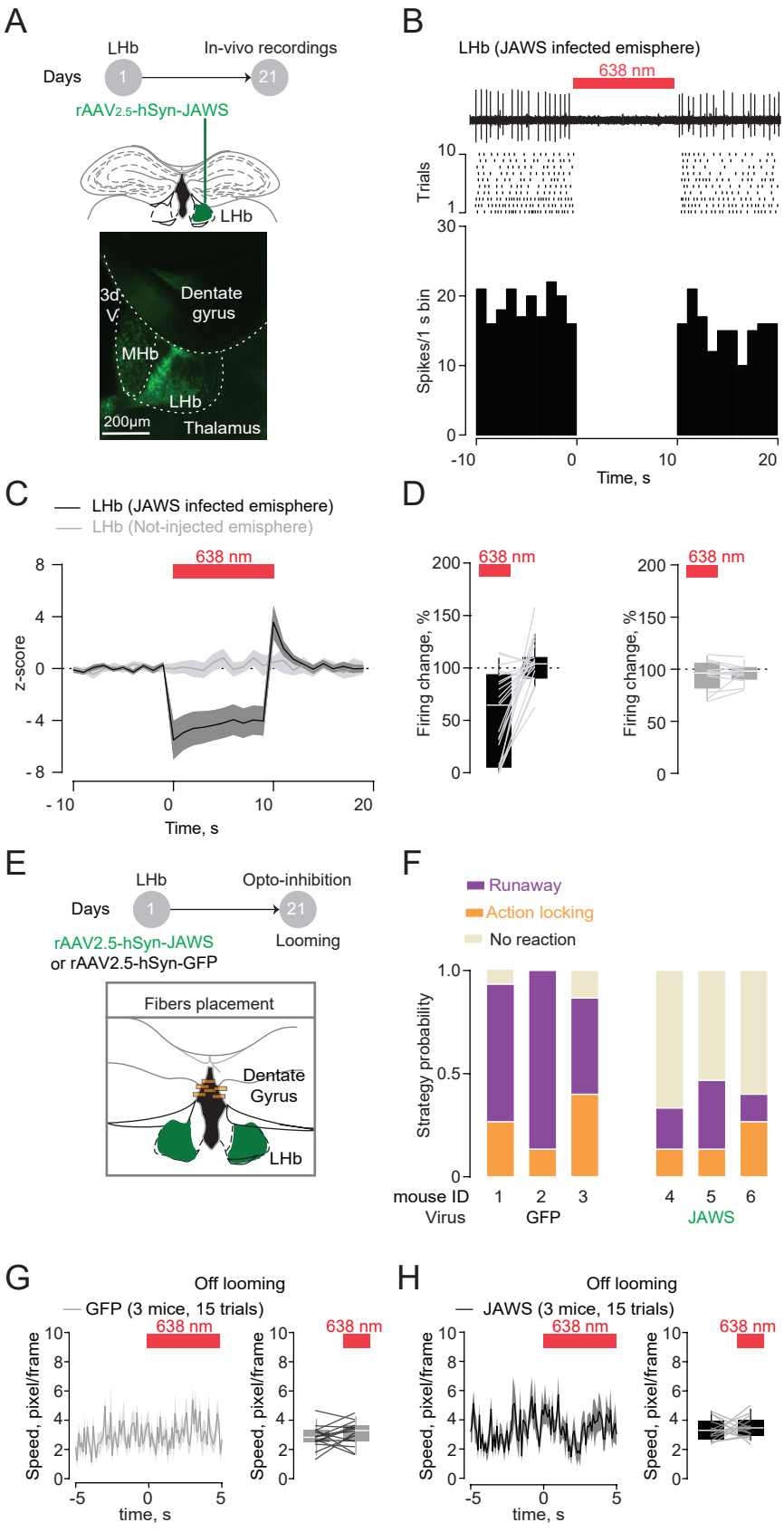
A
LHb
In-vivo recordings
Days
1
21
rAAV2.5-hSyn-JAWS
LHb
3d V.
Dentate gyrus
MHb
LHb
200µm
Thalamus
B
LHb (JAWS infected emisphere)
638 nm
Trials
Spikes/1 s bin
Time, s
C
LHb (JAWS infected emisphere)
LHb (Not-injected emisphere)
638 nm
z-score
Time, s
D
638 nm
Firing change, %
638 nm
Firing change, %
E
LHb
Opto-inhibition
Days
1
21
rAAV2.5-hSyn-JAWS
or rAAV2.5-hSyn-GFP
Looming
Fibers placement
Dentate Gyrus
LHb
F
Runaway
Action locking
No reaction
Strategy probability
mouse ID
Virus
GFP
JAWS
G
Off looming
GFP (3 mice, 15 trials)
638 nm
Speed, pixel/frame
time, s
638 nm
Speed, pixel/frame
H
Off looming
JAWS (3 mice, 15 trials)
638 nm
Speed, pixel/frame
time, s
638 nm
Speed, pixel/frame

Figure S3. LHb silencing during looming-driven defensive responses, Related to Figure 2.
(A) Schematic of the experiment and representative brain coronal section showing JAWS transduction unilaterally in the LHb.
(B) Sample trace, raster plots and peri-stimulus time histogram of a representative LHb neuron in response to 10 trials of 10s continuous red light (638 nm, 8mW).
(C) Averaged z-scored traces (n_{mice}= 3) showing the response to the light activation in the JAWS-infected (23 cells) and not-infected (12 cells) LHb hemisphere (F_{29}= 5.61, ***p<0.0001, Two Way ANOVA RM).
(D) Bar graph and lines reporting the single cell % of change in Firing rate upon the light activation compared to baseline firing (baseline vs light on vs after. Infected hemisphere: 4.51 ± 0.88 Hz vs 3.2 ± 0.93 Hz vs 4.72 ± 0.94 Hz; Bas vs light on: q_{22}= 2.98, *p=0.013; Not-infected hemisphere: 6.12 ± 1.84 Hz vs 6.16 ± 1.89 Hz vs 6.09 ± 1.83 Hz; Bas vs light on: q_{11}= 0.23, p= 0.95; Dunnett's multiple comparisons test).
(E) Schematic of fiber placement in the LHb (brown rectangles represent fiber tip placement).
(F) Bar graph reporting the probability of Runaway (R), Action locking (AL) or no reaction (NR) in response to the looming paired with the light for GFP- (n_{mice}= 3) or JAWS- (n_{mice}= 3) injected mice (GFP_{mouse1}: $n_{runaway}$= 10, $n_{action\ locking}$= 4, $n_{no\ reaction}$= 1. GFP_{mouse2}: $n_{runaway}$= 13, $n_{action\ locking}$= 2, $n_{no\ reaction}$= 0. GFP_{mouse3}: $n_{runaway}$= 7, $n_{action\ locking}$= 6, $n_{no\ reaction}$= 2. X^2_4= 5.8; p= 0.214. $JAWS_{mouse1}$: $n_{runaway}$= 3, $n_{action\ locking}$= 2, $n_{no\ reaction}$= 10. $JAWS_{mouse2}$: $n_{runaway}$= 5, $n_{action\ locking}$= 2, $n_{no\ reaction}$= 8. $JAWS_{mouse3}$: $n_{runaway}$= 2, $n_{action\ locking}$= 4, $n_{no\ reaction}$= 9; X^2_4= 2.622; p=0.623, Chi Square test).
(G) Time-course graph and boxplots depicting the effect of 5s 638nm light activation on the speed of GFP LHb-injected mice (n_{mice} = 3; n_{trials}= 15) during spontaneous locomotion (off looming periods; Baseline (-5s to 0s) vs Light on (0s to 5s): 2.82 ± 0.2 vs 3.09 ± 0.21 pixel/frame; t_{14}= 1.05, p= 0.31, paired t-test).
(H) Same as (G) but for JAWS LHb-injected mice (n_{mice}= 3, n_{trials}= 15; Baseline (-5s to 0s) vs Light on (0s to 5s): 3.29 ± 0.19 vs 3.44 ± 0.19 pixel/frame; t_{14}= 0.45, p= 0.65, paired t-test).

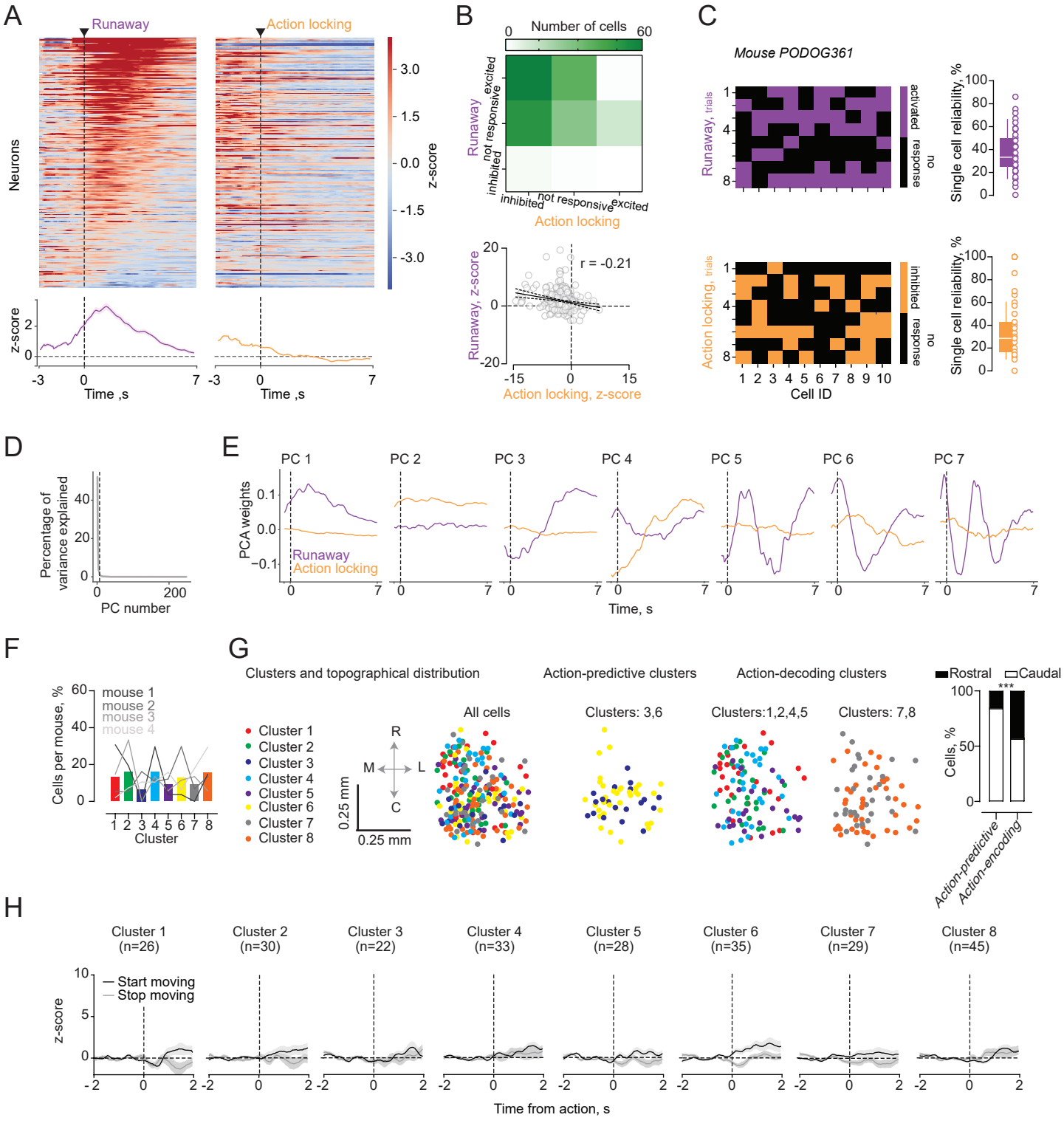
A
Runaway
Action locking
Neurons
z-score
3.0
1.5
0.0
-1.5
-3.0
Time ,s
B
Number of cells
0
60
Runaway
excited
not responsive
inhibited
Action locking
r = -0.21
Runaway, z-score
Action locking, z-score
C
Mouse PODOG361
Runaway, trials
Action locking, trials
activated
inhibited
response
no
Single cell reliability, %
Cell ID
D
Percentage of variance explained
PC number
E
PC 1
PC 2
PC 3
PC 4
PC 5
PC 6
PC 7
PCA weights
Runaway
Action locking
Time, s
F
Cells per mouse, %
mouse 1
mouse 2
mouse 3
mouse 4
Cluster
G
Clusters and topographical distribution
Action-predictive clusters
Action-decoding clusters
Cluster 1
Cluster 2
Cluster 3
Cluster 4
Cluster 5
Cluster 6
Cluster 7
Cluster 8
R
M
L
C
0.25 mm
0.25 mm
All cells
Clusters: 3,6
Clusters:1,2,4,5
Clusters: 7,8
Rostral
Caudal
***
Cells, %
Action-predictive
Action-encoding
H
Cluster 1 (n=26)
Cluster 2 (n=30)
Cluster 3 (n=22)
Cluster 4 (n=33)
Cluster 5 (n=28)
Cluster 6 (n=35)
Cluster 7 (n=29)
Cluster 8 (n=45)
Start moving
Stop moving
z-score
Time from action, s

Figure S4. Single-cell LHb dynamics, cluster detection, topography and their relationship with spontaneous locomotion, Related to Figure 3 and 4.

(A) Mean Ca2+ responses for runaway (left) and action-locking (right) trials time-locked with the behavioral onset, including all cells recorded in 4 mice (n=248). Cells are sorted for response magnitude in runaway trials.
On the bottom, runaway- and action-locking-locked averaged signals. Data are reported as z-score.

(B) On the top, heat-map showing the cell distribution in the different categories according to their response to runaway and action-locking (Runaway/Action-locking: excited/inhibited=73, excited/non responsive=47, excited/excited=4, non responsive/inhibited=62, non responsive/non responsive=35, non responsive/excited=16, inhibited/inhibited=6, inhibited/non responsive=4, inhibited/excited=3). On the bottom, correlation analysis of single cell average Ca2+ responses (z-score) to runaway vs action locking displaying variability (Runaway vs Action-locking; ncells=248, $r=-0.208$; $R^2=0.043$; ***p=<0.0001, Pearson correlation coefficient).

(C) Top: Raster plots showing active (purple squares) and non-active cells (black squares), imaged over different runaway trials in a single mouse. On the right, the boxplot reports single cell reliability (%) for runaway responses (n_{cells}=248, Runaway, 38.01 ± 1.3 %). Bottom, same mouse as top. Raster plots showing cells inhibited (orange squares) or not (black squares), imaged over different action-locking trials. On the right, the boxplot show reliability for single cells in percentage for action-locking responses (n_{cells}= 248, Action-locking, 32.71± 1.37%).

(D) Plot of the percentage variance explained per principal component, showing the number of principal components retained (dashed line).

(E) Individual retained principal components, showing response vectors to both runaway and action-locking trials.

(F) The graph reports the percentage of cells in each cluster (Cluster 1 to 8, number of cells per cluster: 26, 30, 22, 33, 28, 35, 29, 45) and single-mouse contribution per cluster (Cluster 1 to 8, number of cells per cluster. Mouse 1: 16, 10, 0, 7, 3, 6, 7, 3. Mouse 2: 4, 4, 12, 8, 9, 22, 5, 10. Mouse 3: 4, 9, 0, 8, 1, 1, 0, 4. Mouse 4: 2, 7, 10, 10, 15, 6, 17, 28).

(G) Topographical distribution of the clusters in LHb (action-predictive vs action-decoding clusters; rostral vs caudal cell distribution; Action-predictive: 57 cells, 9 rostral vs 48 caudal. Action-decoding: 191 cells, 83 rostral vs 108 caudal. $X^2_1= 14.4$; $z=3.79$; ***p=0.0001, Chi-Square test).

(H) Average traces across all neurons within cluster aligned to the start (black traces) or stop (gray traces) moving onset.